machines

MDPI

Article

Condition Monitoring Technology and Its Testing for 5G-Enabled High-Speed Railway Wireless Communication Networks: Guaranteeing the Reliability of Train–Ground Communication

Cheng Li [1,2], Pengyu Ren [1,2], Dan Fei [1,2], Bo Ai [1,2] and Lei Xiong [1,*]

[1] The State Key Laboratory of Advanced Rail Autonomous Operation, Beijing Jiaotong University, Beijing 100044, China; chengli@bjtu.edu.cn (C.L.)
[2] School of Electronic and Information Engineering, Beijing Jiaotong University, Beijing 100044, China
* Correspondence: lxiong@bjtu.edu.cn

Abstract

Currently, fifth-generation (5G) communication has emerged as the most promising candidate for next-generation railway-dedicated communication systems. Condition monitoring of 5G networks is critical for ensuring the continuity and reliability of train–ground communications. In this paper, a real-time monitoring technology is proposed, which is based on generalized channel characteristics extracted from received Demodulation Reference Signals (DM-RSs). Furthermore, a corresponding monitoring system has been developed based on the Radio Frequency System on Chip (RFSoC). Experimental results demonstrate that the proposed condition monitoring system exhibits excellent performance: it can accurately measure key network metrics (including field strength, multipath components, and frequency offset) and enable real-time monitoring of the operational condition of 5G radio access networks (RAN) and on-board terminals. Future work will focus on integrating the monitoring system into on-board terminals.

Keywords: high-speed railways; 5G; train-ground communication; channel; monitoring; RFSoC

check for updates

Academic Editor: Davide Astolfi

Received: 29 October 2025
Revised: 16 November 2025
Accepted: 19 November 2025
Published: 25 November 2025

Citation: Li, C.; Ren, P.; Fei, D.; Ai, B.; Xiong, L. Condition Monitoring Technology and Its Testing for 5G-Enabled High-Speed Railway Wireless Communication Networks: Guaranteeing the Reliability of Train–Ground Communication. *Machines* **2025**, *13*, 1087. https://doi.org/10.3390/machines13121087

Copyright: © 2025 by the authors. Licensee MDPI, Basel, Switzerland. This article is an open access article distributed under the terms and conditions of the Creative Commons Attribution (CC BY) license (https://creativecommons.org/licenses/by/4.0/).

1. Introduction

Railways have played an important role in the modern world. Currently, the railway is advancing from the information era to the intelligent era. The intelligent railways can realize comprehensive sensing, ubiquitous interconnection, and integrated processing of railway equipment, infrastructure, and environmental information [1].

Railway-dedicated communication systems serve as the backbone of modern rail transport, enabling real-time communication between trains, operators, and control centers while ensuring the safety, reliability, and efficiency of train operations. Thus, the robust and efficient communication system has become increasingly critical [2,3].

In recent years, the new communication services are emerging continuously, including train operation control, train condition monitoring, video surveillance, and intelligent dispatching. Existing GSM-R, as a narrowband communication system, fails to meet the requirements of such intelligent railway services [4,5]. Additionally, with the gradual decommissioning of the GSM public network, GSM-R is also confronting the risk of industrial chain disruption. The Future Railway Mobile Communication System (FRMCS) [6,7], proposed by the International Union of Railways (UIC), serves as a key enabler for the evolution of future railway communication systems.

Endowed with ultra-low latency, high capacity, support for the massive Internet of Things (IoT), and high security, fifth-generation (5G) communication has emerged as the most promising candidate technology for next-generation railway dedicated communication, and thus attracted more and more attention [8,9].

The European Union (EU) has launched the 5GRAIL project to advance the application of 5G technology in railway scenarios [10]. Additionally, NTT DOCOMO and East Japan Railway Company have verified the stable operation of typical 5G communication capabilities in railway environments, while the Korea Railroad Research Institute (KRRI) has conducted tests on 5G-based autonomous train control technology. China has proposed the development of the dedicated mobile communication network for high-speed railways based on public-network 5G technology, i.e., 5G-R [11].

The faults occurring in the railway-dedicated mobile communication network may result in operation speed reduction and even complete train stoppages, severely impacting the safety and efficiency of train operations [12,13].

The Network Management System (NMS) enables network engineers to perform several key operations for the core network and bearer network, including performance monitoring, performance analysis, device detection, and alert notifications [14–17].

It has been estimated that over 70% of all service degradations are due to issues in the Radio Access Network (RAN), including faults in power amplifiers, suboptimal antenna alignment, poor RF connections, and drift of the local oscillator frequency. These degradations have a critical impact, including lack of connectivity, dropped calls, and slow transmission speeds.

Currently, the primary method for detecting such failures primarily relies on the comprehensive inspection train (CIT). Equipped with specialized inspection systems—including those for track, contact line, communication networks, and signaling systems—CIT perform regular assessments of the high-speed rail infrastructure to identify potential safety hazards and defects [18–23].

Typical examples of CIT include the Manned Ground Vehicle (MGV) operated by the French National Railway Company (SNCF); the "Archimede" high-speed comprehensive inspection train developed by Meridional Meccanica (MER MEC) in Italy; the "East-i" inspection train utilized in Japan; and China's new-generation CIT450 high-speed comprehensive inspection train [24].

However, the CIT exhibits the following limitations:

(1) Due to the high operation cost and limited quantity of CITs, the detection cycles are relatively long (typically 10–15 days), making it difficult to achieve real-time monitoring of the high-speed railway wireless communication network.
(2) Comprehensive track inspection vehicles lack the capability to detect faults in on-board terminals, including malfunctions in on-board antennas and RF feeder lines. The CIT is incapable of detecting faults in the on-board terminal, such as malfunctions in on-board antennas and RF feeder lines.

To address this issue, we propose a condition monitoring perception system for 5G-R RAN and on-board terminal to ensure communication reliability. Generalized channel characteristics are extracted from the received Demodulation Reference Signals (DM-RSs), including key parameters such as field strength, multipath delay, and frequency offset.

As opposed to the traditional channel—defined as the radio signal transmission from the transmitting to the receiving antenna [25–27]—the generalized channel encompasses the entire chain from the modulator output, through the RF transmitter (including the power amplifier), transmitting antenna, wireless propagation, and receiving antenna, to the demodulator input. Consequently, the characteristics of the generalized channel reflect

not only the radio propagation but also the properties of the transmitting and receiving modules and equipment.

High-speed trains operate on fixed tracks, and at each specific location, signal propagation does not change drastically, i.e., channel characteristics exhibit high regularity. However, when equipment faults occur, it will lead to severe deterioration of the channel. Taking the received field strength as an example, when an equipment fault happens, the received field strength may decrease by several decibels (dB) or even dozens of dB, while the measurement error is much lower (not exceeding 0.2 dB, as shown in Section 6). Therefore, through the comparative analysis of generalized channel characteristics extracted from the received signal and pre-stored generalized channel characteristics under normal conditions, the developed monitoring system is capable of distinguishing equipment faults of the radio access network (RAN) in 5G-R networks from signal propagation changes in system self-errors.

In this paper, a real-time condition monitoring system for the 5G network based on the Radio Frequency System on Chip (RFSoC) is developed. This system supports the Sub-6 GHz frequency band, a 1 GHz bandwidth, and 8 receiving antennas, and can not only meet the requirements of the current 5G dedicated mobile communication networks and public networks, but also cater to the development needs of future networks. Experimental results demonstrate that the developed system exhibits high measurement accuracy and strong application adaptability. Compared with the existing CIT-based method, the proposed method exhibits the following advantages:

(1) The system indeed requires complex signal processing, including radio frequency (RF) sampling, control-channel decoding, and channel characteristic extraction. However, the system only comprises a receiver; most of the processing procedures are fully implemented via software algorithms, and can be integrated into on-board terminals in the future. The system has a simple structure and low cost, and can be deployed on in-service high-speed trains, thereby enabling long-term real-time monitoring of the high-speed railway wireless network.
(2) The system not only monitors the RAN but also the on-board terminals of high-speed trains.
(3) The system reuses the on-board antenna and RF feeder, so the measurement results are more consistent with the actual situation.

The reminder of this paper is organized as follows: Section 2 introduces the system model and reference signals. Section 3 proposes the network metrics extraction method. Section 4 presents the details of system design and implementation of the RFSoC-based network monitoring system. Section 5 presents the experimental results. Finally, Section 6 provides the concluding remarks.

2. Framework

2.1. System Architecture

The system model of the 5G network monitoring system proposed in the paper is shown in Figure 1.

The 5G network monitoring system is installed on a high-speed train. The 5G signals received by the on-board antenna array are split into two parts by the RF coupler: one part is used for the normal communication of the on-board 5G terminal, and the other part is input into the 5G network monitoring system.

In the system, the core board samples and processes RF signals to obtain the In-phase/Quadrature (I/Q). This data is then transmitted to the host computer for data

analysis, where network performance metrics are extracted to realize the monitoring of the 5G network status.

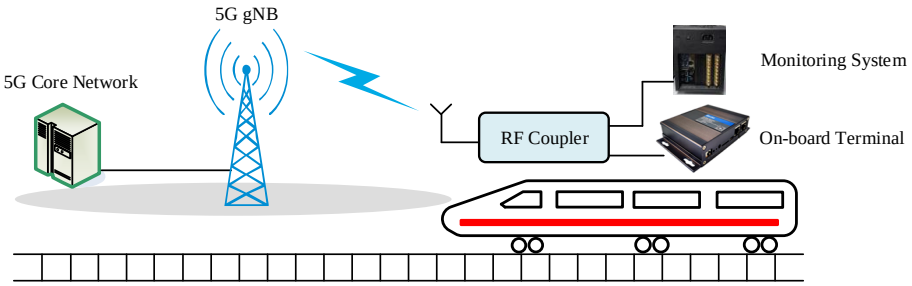


Figure 1. The system model of the 5G network monitoring system.

2.2. Reference Signals

In the 5G system, the Primary Synchronization Signal (PSS), Secondary Synchronization Signal (SSS), and Demodulation Reference Signals (DM-RSs) are known to the receiver. Thus, the basic principle of the proposed method is to obtain the network by comparing the received signals and transmitted signals mentioned above [28].

PSS provides coarse synchronization regarding frequency and timing, and SSS offers fine synchronization, and works with PSS to create the Physical Cell ID (PCI), that is PCI = 3 × NID1 + NID2.

In 5G NR, the combination of SS and Physical Broadcast Channel (PBCH) is known as Synchronization Signal and PBCH block, which plays a crucial role in cell search and mobility.

As shown in Figure 1, SSB is mapped to 20 RBs (i.e., 240 subcarriers) in the frequency domain and 4 OFDM symbols in the time domain. And PSS occupies 127 subcarriers sequentially from subcarrier 56 to 182 in the OFDM symbol 0, and SSS also occupies 127 subcarriers in the OFDM symbol 2.

PBCH spans OFDM symbols 1 and 3 (subcarrier 0–239) and parts of OFDM symbol 2 (subcarrier 0–47 and 192–239). DM-RS is a special type of reference signal used to estimate the channel for demodulation, and widely present in various important physical channels, such as the downlink PBCH, PDCCH, and PDSCH.

As shown in Figure 2, the DM-RS for PBCH is mapped to OFDM symbol 1 and 3 with its subcarrier number ranging from $0 + v$ to $239 + v$, and mapped to OFDM symbol 2 with its subcarrier number ranging from $0 + v$ to $44 + v$, and $192 + v$ to $239 + v$, where the variable v is calculated as a function of the physical cell ID modulo 4.

PSS and SSS only occupy 127 consecutive subcarriers in the middle of the SSB in the frequency domain, and the frequency domain coverage is narrow. Therefore, it is impossible to evaluate the channel very finely. Although the DM-RS signal only occupies 1/4 of the subcarriers in the PBCH (60 subcarriers in symbols 1 and 3, and 24 subcarriers in symbol 2), due to its comb-like characteristics, it has a wider distribution in the entire frequency domain, so it has better estimation accuracy. Therefore, this paper selects the DM-RS signal for channel estimation.

DM-RS is distributed on three downlink physical channels: Physical Downlink Shared Channel (PDSCH), PBCH, and Physical Downlink Control Channel (PDCCH). PDSCH is the main downlink data-bearing channel in 5G, which is used to transmit user data and upper-layer signaling, occupying most of the subcarriers and Orthogonal Frequency Division Multiplexing (OFDM) symbols in the downlink signal, and the filling density of DM-RS in it is relatively high, occupying a larger bandwidth. Therefore, this paper uses the DM-RS in PDSCH for channel estimation.

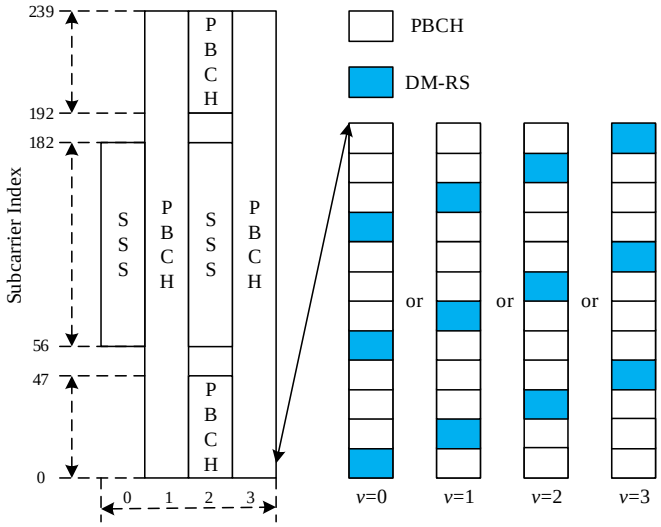


Figure 2. Time-frequency structure of the PSS/SSS/PBCH.

The DM-RS in PDSCH is generated by the following recursive formula:

$$r(n) = \frac{1}{\sqrt{2}}(1 - 2 \cdot c(2n)) + j\frac{1}{\sqrt{2}}(1 - 2 \cdot c(2n+1)) \quad (1)$$

where $c(i)$ is a pseudo-random sequence (Gold sequence).

The pseudo-random sequence generator shall be initialized with

$$c_{init} = (2^{17}(N_{symb}^{slot} n_{s,f}^{\mu} + l + 1)(2N_{ID}^{n_{SCID}} + 1) + 2N_{ID}^{n_{SCID}} + n_{SCID}) mod 2^{31} \quad (2)$$

where l is the OFDM symbol number within the slot, $n_{s,f}^{\mu}$ is the slot number within a frame, N_{symb}^{slot} is the number of OFDM symbol number within the slot, $N_{ID}^{n_{SCID}}$ is scrambling identity range from 0 to 65,535, If the scrambling ID is not set, N_{ID}^{SCID} defaults to the cell ID N_{ID}^{cel}, $n_{SCID} \in \{0, 1\}$ is given by the DM-RS sequence initialization field.

In the time domain, DM-RS does not occupy all the OFDM symbols of PDSCH, but occupies certain OFDM symbols; in the frequency domain, the DM-RS signal is inserted into the determined subcarriers in a comb-like form in PDSCH.

Since the DM-RS signal is known to the receiver, channel estimation can be performed by comparing the locally generated DM-RS signal with the received DM-RS signal, determining the frequency-domain response on the subcarriers where the DM-RS is located, obtaining the channel impulse response (CIR) through Inverse Fast Fourier Transform (IFFT), and then extracting network metrics such as the covered field strength, multipath, and frequency offset, to achieve the monitoring of the 5G wireless network in high speed railway.

Furthermore, unlike the 5G mobile communication systems deployed in public networks, the 5G-R system bears core services, including train operation control, real-time train status monitoring, and on-board train video surveillance. These services are required to maintain continuous online availability throughout the entire train operation process. Consequently, real-time monitoring based on PDSCH DM-RS is reliable.

3. Network Metrics

(1) Covered Field Strength

Field strength—i.e., the received signal strength (RSS)—is one of the most important parameters for wireless networks. Insufficient coverage field strength may lead to poor

transmission reliability. And unfavorable coverage field strength at cell edges constitutes a primary cause of handover failure. Accordingly, the proposed system facilitates accurate monitoring of coverage field strength, thereby enhancing transmission reliability and mitigating handover failure [29,30].

When wireless network failures occur—such as power amplifier faults, antenna faults, and poor RF feeder connections in base stations or on-board equipment—the coverage field strength may decrease by several decibels (dB) or even dozens of dB.

(2) Multipath

In radio propagation, radio signals are not only transmitted via line-of-sight, but also through multiple other mechanisms (e.g., reflection, diffraction, and scattering) owing to the presence of obstacles and scatterers in the propagation environment. Notably, the multipath components of distinct propagation mechanisms exhibit different delays and powers [31,32].

To improve transmission performance and extend coverage range, 5G systems typically rely on directional antennas or antenna arrays to form narrow beams. When the beams in base stations or on-board terminals deflect or are blocked by obstacles, it causes changes in multipath, including the number of multipaths, delay and power and fading distribution of each path.

(3) Frequency Offset

Local oscillator frequency drift in the base station and Doppler shift induced by the high-speed movement of trains will both give rise to frequency offset, and such frequency offset will significantly degrade the transmission performance of 5G communication systems [33,34]. Furthermore, the train operation speed generally remains constant at a specific position; for instance, the speed is zero when the train is stopped at a station, and reaches a maximum of 350 km/h when operating on the mainline. Therefore, the Doppler effect is basically deterministic. Thus, it is feasible to distinguish oscillator drift from the Doppler effect.

4. Network Metrics Extraction Based on DM-RS

The diagram of the network metrics extraction based on DM-RS signals is shown in Figure 3 and introduced below.

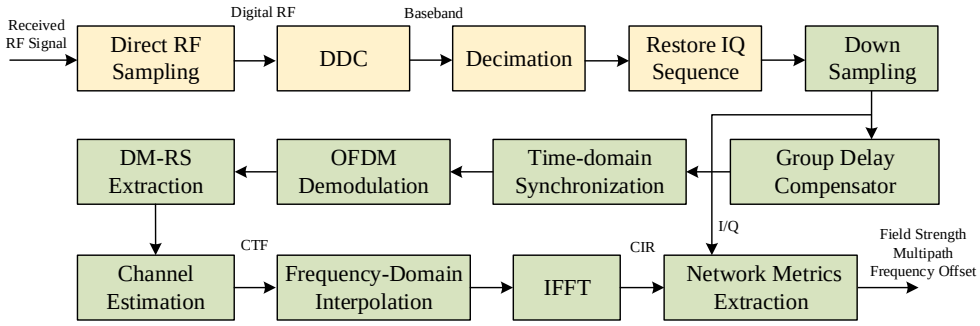


Figure 3. The diagram of network metrics extraction based on DM-RS signals. (Note: The blocks marked in yellow are executed on the Core Board, while those marked in green are executed on the host computer).

4.1. Direct RF Sampling

In a traditional heterodyne receiver, the RF signal is generally down-converted to a lower intermediate frequency (IF) or baseband by one or more stages, then Analog-to-Digital Conversion is performed, followed by subsequent digital processing. As shown in

Figure 4, the RF front end of the heterodyne receiver consists of a bandpass filter, low-noise amplifier, mixer, and local oscillator (LO).

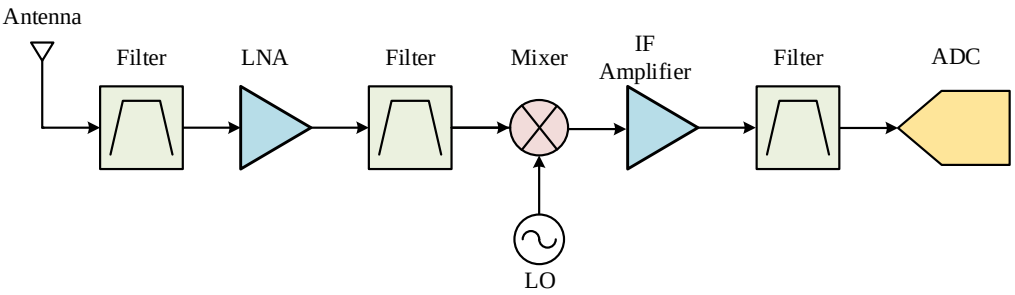


Figure 4. The architecture of heterodyne receiver.

However, non-ideal characteristics of RF analog devices in the RF front, such as phase noise, LO leakage, spurs, and harmonics, will affect the measurement accuracy. To improve the accuracy of channel characteristic measurement, this paper adopts a scheme of direct RF sampling [35,36]. As shown in Figure 5, a direct RF sampling receiver consists of just a low-noise amplifier, the filters, and the Analog-to-Digital Converter (ADC), and directly samples the RF signal. The direct RF sampling receiver is much simpler, thus minimizes the impact of the non-ideal characteristics of RF devices on the measurement accuracy.

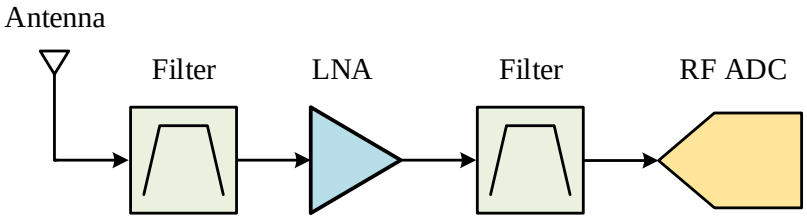


Figure 5. The architecture of the direct RF sampling.

The monitoring system directly samples the received RF signal $r(t)$ that has experienced wireless channel transmission at the low-pass Nyquist sampling frequency,

$$r[n] = r(nT_s) \tag{3}$$

where T_s is the sampling interval, and $T_s = 1/f_s$,f_s is the RF signal sampling rate. According to the Nyquist-Shannon sampling theorem, to recover the original signal $r(t)$ without distortion, it must satisfy $f_s \geq 2f_m$, where f_m is the highest frequency of the signal, and $2f_m$ is also called Nyquist rate.

However, the RF signals are typically bandpass signals. If sampled at the Nyquist rate, it will require ultra-high ADC sampling rate, and the existing ADC is difficult to meet the requirements.

In the actual design and implementation, undersampling technology is adopted. By using the aliasing phenomenon, the target signal is deliberately folded into the first Nyquist zone so as to sample the high-frequency bandpass signal with a lower sampling frequency, greatly saving the system complexity, cost, and power consumption. In our design, the sampling rate $f_s = 4.9152$ GSa/s.

4.2. Digital Down Conversion

The digital down conversion (DDC) is to convert the RF digital signal from the center frequency f_c to a low-frequency or baseband signal for subsequent processing. DDC usually includes two steps, digital mixing and low-pass filtering.

The signal after down-conversion can be expressed as

$$r[n] = r_{RF}[n] \times c[n] \tag{4}$$

where $c[n] = e^{-j2\pi n f_c / f_s}$ is the local oscillator signal. At the output of digital mixer, a low-pass filter is used to filter high-frequency components.

4.3. Decimation

In order to reduce the sample rate and processing complexity, the signal after digital down-conversion is decimated. The decimated signal is

$$r^{'}[m] = r[m \cdot D] \tag{5}$$

where D is the decimation factor, and is related to the measurement bandwidth. For example, in our design, $D = 40$, when the measurement bandwidth is 100 MHz. That is, after decimation, the sampling rate is reduced to 122.88 MSa/s. And an anti-aliasing digital filter precedes the decimation to prevent aliasing from occurring, due to the lower sampling rate.

4.4. Restore I/Q Sequence

In the digital processing board, the sampling data is temporarily stored in the Dynamic Double Rate 4 (DDR4) Random Access Memory (RAM) through the Peripheral Component Interconnect express (PCIe) interface. The host computer reads the sampling data from the RAM and restores I/Q sequences of each ADC channel.

4.5. Downsampling and Group Delay Compensator

To flexibly adjust the system's measurement bandwidth without adjustment to core board configurations, when the measurement bandwidth is relatively small, downsampling can be performed on the I/Q sequence in the host computer by software. This further reduces the sampling rate and lowers the system complexity. For instance, when the sampling rate of the core board is 122.88 MSa/s, the sampling rate can be reduced to 15.36 MSa/s through 8× downsampling, which is adequate to meet the measurement requirement for 10 MHz bandwidth.

To avoid aliasing during downsampling, anti-aliasing filtering needs to be performed in advance. Additionally, group delay compensation is also required to compensate for the group delay caused by the anti-aliasing filtering.

4.6. Time-Domain Synchronization

As shown in Equation (1), the DM-RS is generated based on the Gold sequence and exhibits superior auto-correlation and cross-correlation properties. Accordingly, time-domain synchronization is achieved via correlation computations, thereby determining the starting position of the OFDM symbol within the received signal.

For simplicity, without consideration of noise, the time-domain sequence of a received OFDM symbol can be expressed as

$$r[k] = \frac{\sum_{m=0}^{N-1} h[m]x[m]e^{j\frac{2\pi}{N}mk}}{N}, k = 0, 1 \cdots N-1 \tag{6}$$

where N is the number of OFDM subcarriers, $x[m]$ and $h[m]$ represent the signal and frequency response on the m-th subcarriers, respectively.

In the PDCCH, DM-RS only occupies a portion of its subcarriers, while most of the remaining subcarriers carry data symbols. Since the monitoring system only knows the value of the DM-RS but not the values of the data symbols, zeros are filled in the positions of these subcarriers in this design, shown in Figure 6.

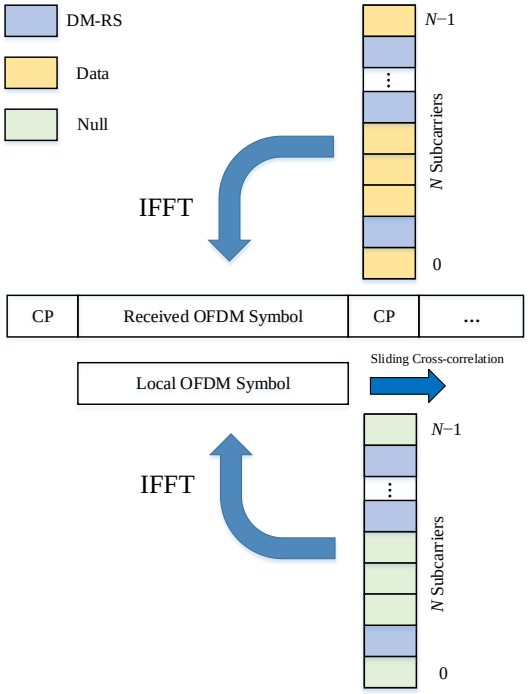


Figure 6. The schematic diagram of time-domain synchronization.

Therefore, the time-domain sequence of a locally generated OFDM symbol (referred to as the reference signal sequence) can be expressed as

$$ref[k] = \frac{\sum_{m=0}^{N-1} x'[m] e^{j\frac{2\pi}{N}mk}}{N}, k = 0, 1 \cdots N-1 \tag{7}$$

where $x'[m] = \begin{cases} x[m] & m \in S_{\mathrm{DM-RS}} \\ 0 & m \notin S_{\mathrm{DM-RS}} \end{cases}$ is the set of the subcarriers occupied by DM-RS. Prior to the completion of synchronization, the monitoring system is unable to ascertain the starting position of an OFDM symbol.

The sliding cross-correlation value between the locally generated reference signal ref and the received signal r can be expressed as

$$\begin{aligned} R_{r,ref}[n] &= \sum_{k=0}^{N-1} ref[k] r^*[k+n] \\ &= \sum_{k=0}^{N-1} \left(\frac{\sum_{m=0}^{N-1} x'[m] e^{j\frac{2\pi}{N}mk}}{N} \times \frac{\sum_{m=0}^{N-1} h^*[m] x^*[m] e^{-j\frac{2\pi}{N}m(k+n)}}{N} \right) \end{aligned} \tag{8}$$

Without loss of generality, it can be assumed that when $n = 0$, the locally generated reference signal ref achieves synchronization with the received signal r, and the cross-correlation value is calculated as

$$\begin{aligned} R_{r,ref}[0] &= \sum_{k=0}^{N-1} ref[k]r^*[k] \\ &= \sum_{k=0}^{N-1} \frac{\sum_{m=0}^{N-1} x'[m]e^{j\frac{2\pi}{N}mk}}{N} \times \frac{\sum_{m=0}^{N-1} h^*[m]x^*[m]e^{-j\frac{2\pi}{N}mk}}{N} \\ &= \frac{1}{N^2} \sum_{k=0}^{N-1} \sum_{m'=0}^{N-1} \sum_{m=0}^{N-1} x'[m']h^*[m]x^*[m]e^{j\frac{2\pi}{N}(m'-m)k} \end{aligned} \tag{9}$$

Due to the orthogonality between subcarriers,

$$\sum_{m=0}^{N-1} e^{j\frac{2\pi}{N}mk_1}e^{-j\frac{2\pi}{N}mk_2} = \sum_{m=0}^{N-1} e^{j\frac{2\pi}{N}m(k_1-k_2)} = \begin{cases} N, k_1 = k_2 \\ 0, k_1 \neq k_2 \end{cases} \tag{10}$$

It can be obtained that

$$R_{r,ref}[0] = \frac{1}{N} \sum_{m \in S_{\mathrm{DM-RS}}} h^*[m]|x[m]|^2 \tag{11}$$

Due to the superior auto-correlation and cross-correlation properties of the DM-RS, cross-correlation value $R_{r,ref}[n] \approx 0, n \neq 0$.

Clearly, $R_{r,ref}[n]$ is close to the Dirac Delta function, which is confirmed by the measured data presented in Figure 7.

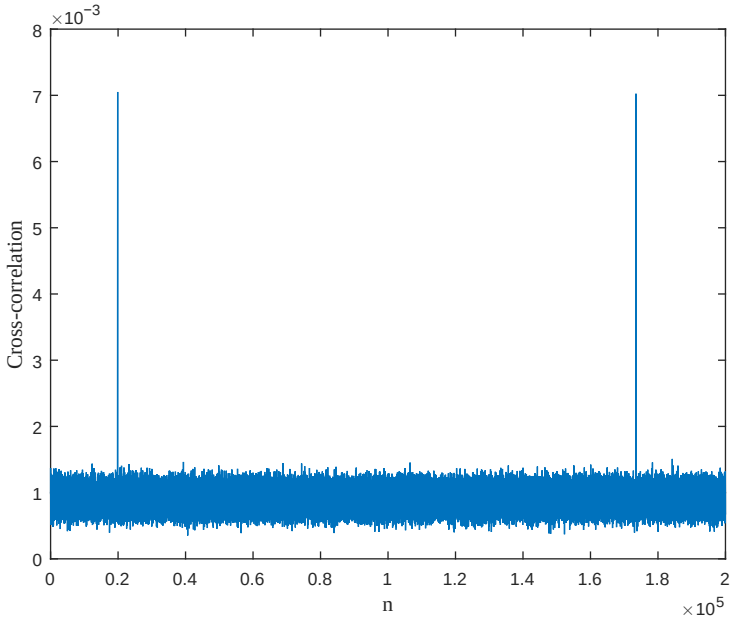


Figure 7. Cross-correlation value of the measured data.

4.7. OFDM Demodulation

Following the determination of the OFDM symbol start point via time-domain synchronization, the soft decision result of OFDM demodulation is derived through the sequential execution of cyclic prefix removal, serial-to-parallel conversion, and FFT processing.

4.8. DM-RS Extraction

On the basis of the 5G frame structure and the restored resource grid, the received DM-RS are extracted from the corresponding subcarriers.

4.9. Channel Estimation

Based on the received DM-RS, the frequency domain response on the subcarrier where DM-RS is located, is calculated as follows:

$$\hat{H[t,m]} = \frac{r[t,m]}{ref[t,m]}, m \in S_{\mathrm{DM-RS}} \tag{12}$$

where $r_{\mathrm{DM-RS}}[t,m]$ and $x_{\mathrm{DM-RS}}[t,m]$ are the values of the received and locally generated DM-RS on the m-th subcarrier at time t, respectively.

4.10. Frequency-Domain Interpolation

The DM-RS signals are distributed in the time-frequency domain in comb-like form, the frequency-domain responses obtained by Equation (12) are on discrete subcarriers. In our design, the linear interpolation method is used to obtain the channel transfer function (CTF) over the entire bandwidth.

The interpolated value of the frequency-domain response on the k-th subcarrier at time t without DM-RS is

$$\hat{H[t,k]} = \hat{H[t,i]} + \frac{\hat{H[t,j]} - \hat{H[t,i]}}{j-i}(k-i) \tag{13}$$

where j and i are the indices of two adjacent subcarriers within DM-RS, and $i < k < j$.

4.11. CIRs Obtain

Performing Inverse Fast Fourier Transform (IFFT) on the interpolated channel transfer function domain response results can generate the channel impulse response CIR at time t, and the expression is

$$\hat{h}[t, n\Delta\tau] = \frac{1}{N}\sum_{k=0}^{N-1} \hat{H}[t,k] e^{j\frac{2\pi}{N}kn} \tag{14}$$

where N is the number of OFDM subcarriers, $\Delta\tau$ is the delay resolution, and $\Delta\tau = 1/B$, B is the system bandwidth.

4.12. Network Metrics Extraction

Based on the CIRs and I/Q data, the key network metrics—including covered field strength, multipath delay, and frequency offset—can be further extracted.

(1) Covered Field Strength

The instantaneous power of the received signal is calculated as

$$P[k] = \frac{r_{\mathrm{I}}^2[k] + r_{\mathrm{Q}}^2[k]}{R} \tag{15}$$

where $r_{\mathrm{I}}[k]$ and $r_{\mathrm{Q}}[k]$ are the sampling values of the in-phase (I) and quadrature (Q) components of the received signal at time k, and R is the Characteristic Impedance, $R = 50$.

Covered field strength is defined as the time expectation of the $P[k]$,

$$\bar{P} = E_t[P[k]] \tag{16}$$

(2) Multipath

For convenience in practical applications, typically only the multipath components with relatively higher power in the CIRs are retained as effective multipath components, whereas those with relatively low power (e.g., components whose power is more than 20 dB or 30 dB lower than that of the maximum-power component) are neglected.

The coefficient, delay and power of the effective multipath components can be, respectively, expressed as follows:

$$\begin{cases} h_{\text{eff}}[t,\tau] = \hat{h}[t,n\Delta\tau] \\ \quad \tau = n\Delta\tau, \qquad \text{if } \left|\hat{h}[t,n\Delta\tau]\right|^2 \geq \alpha \max_n \left|\hat{h}[t,n\Delta\tau]\right|^2, n = 0,1,\cdots,N-1 \\ P_\tau = E_t\left[\left|\hat{h}[t,n\Delta\tau]\right|^2\right] \end{cases} \tag{17}$$

where α is the power threshold coefficient, and $E_t[\,]$ is expectation in the time domain.

(3) Frequency Offset

The Doppler spectrum of the multipath component with the strongest power is obtain by FFT processing,

$$S[f,\tau'] = \int_{-\infty}^{+\infty} h_{\text{eff}}[t,\tau']e^{-j2\pi ft}dt \tag{18}$$

where $h_{\text{eff}}[t,\tau']$ is the multipath component with the maximum power. And frequency Offset $f_{\text{offset_max}}$ is the maximum effective value of the Doppler spectrum.

5. System Design and Implementation

In this section, the design and implementation of the 5G network monitoring system are introduced.

The diagram of the system is shown in Figure 8, and the system is composed of the core board and host computer. And the core board is consist of ADC, Field Programmable Gate Array (FPGA), clock module, power supply module IC, peripheral DDR4 RAM, and host computer, etc.

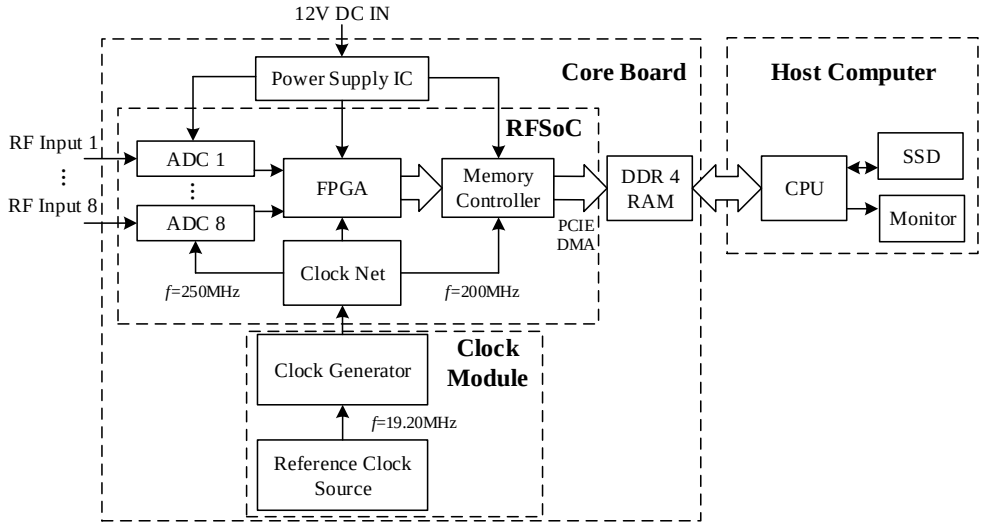


Figure 8. The hardware architecture of the 5G network monitoring system.

(1) ADC

According to the bandpass sampling theorem, the sampling rate of ADC must be greater than twice the signal bandwidth, that is, $F_s \geq 2\,\text{B}$. Considering the influence of the

roll-off, in fact, the sampling rate of ADC is generally greater than 2.4 B. The parameters of four ADC chips, AD9081 from Analog Devices Inc. (ADI) in Norwood, Massachusetts, United States, ADC12J4000 from Texas Instruments (TI) in Dallas, Texas, United States, and XCZU27DR and XCZU47DR from Xilinx in San Jose, California, United States, are compared in Table 1. As shown in the table, XCZU47DR not only has 8 ADC channels, each with a 14-bit resolution and a sampling rate of up to 5 GS/s, but also integrates a high-performance FPGA. Using this chip not only saves costs, reduces the development difficulty, and reduces power consumption, but also realizes miniaturized design, with obvious advantages.

(2) FPGA

In the design, the built-in FPGA of the XCZU47DR device is employed to execute data processing tasks for the 8-channel ADC sampled signals, including digital down conversion (DDC), decimation, anti-aliasing digital filter, cascading, and format conversion.

Table 1. Chip parameters comparison.

	Chip	**AD9081**	**ADC12J4000**	**XCZU27DR**	**XCZU47DR**
ADC	Number of ADCs	4	1	8	8
	Resolution (Bits)	16	12	12	14
	Maximum Sampling Rate (GS/s)	4	4	4	5
FPGA	Logic Cells (K)	none	none	930	930
	DSP Slices	none	none	4272	4272
	Memory (MB)	none	none	60.5	60.5

(3) DDR4 RAM

In this design, the data processed by the FPGA is temporarily stored in the DDR4 RAM.

(4) Clock circuit

The clock module guarantees the synchronization of all on-circuit signals across the entire circuit, while timing constraints ensure that signals meet required deadlines for data propagation.

Given the multiple clocks with distinct frequency requirements in the system, the principle of minimizing the number of external high-frequency clocks is followed. Thus, a low-jitter and low-phase-noise reference clock signal in 19.2 MHz is obtained by a high-performance crystal oscillator and Phase Locked Loop (PLL) in the clock jitter eliminator.

Subsequently, through the built-in clock network in RFSoC XCZU47DR, frequency multiplication, frequency division, buffering, biasing and other processes are completed to obtain clock signals with different frequencies and forms for different modules on the system, as shown in Table 2.

Table 2. List of clocks in core board.

Clock	**Frequency**
Internal Reference Clock	19.20 MHz
ADC Reference Clock	250 MHz
SYSREF Clock	10 MHz
FPGA Global Clock	122.88 MHz
DDR4 RAM	200 MHz
PCIe Working Clock	250 MHz

(5) Power Supply Circuit

In the system, a high-performance power supply chip is used to convert the 12 V Direct Current (DC) power supply into common power rails and dedicated power rails. The dedicated power rail provides power to the RFSoC chip XCZU47DR, while the common power rail is responsible for supplying power to peripheral circuits such as the clock circuit and DDR4 RAM.

XCZU47DR is the core component in the board with the highest power consumption. Power Design Manager (PDM), which is a new generation of power consumption estimation platform from Xilinx, is employed to estimate the power requirements of XCZU47DR.

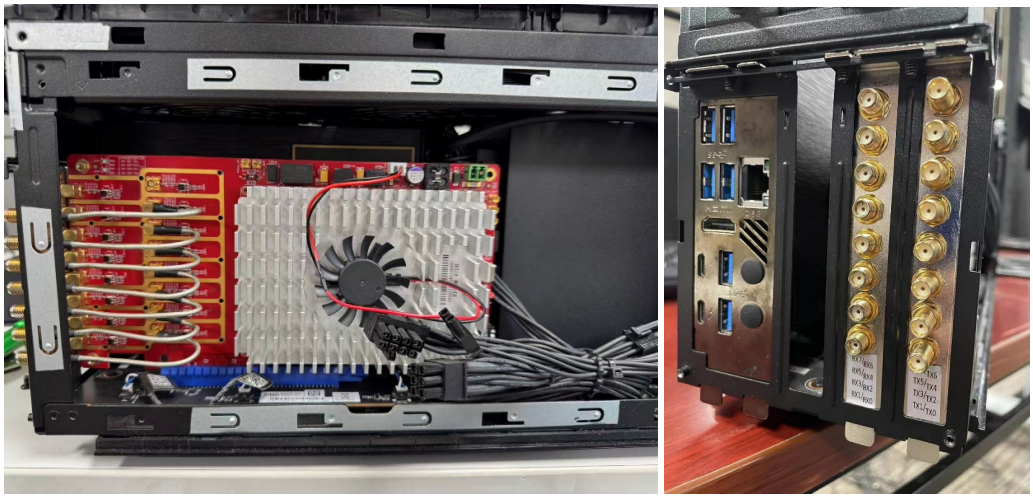
It is estimated that the required power supply voltage for the main power supply of XCZU47DR is 0.8 V, and the current is approximately 15.7 A. Therefore, the LTM4650IY#PBF power supply chip from Analog Devices is selected. Its input voltage is 4.5–15 V, output voltage is 0.6–1.8 V, and output current is 25–50 A, which can meet the voltage and current requirements of power rails on the board.

(6) Host Computer

The host computer in this paper is configured as follows: Intel Core i7-11700B CPU, GeForce RTX 3060 GPU, 4 GB of RAM, 2 TB Solid State Disk (SSD), and 2.5 GbE + Gigabit Ethernet ports.

The host computer undertakes the following tasks: (1) reading the measurement data temporarily cached in the RAM; (2) performing signal processing, including downsampling, group delay compensation, signal synchronization, OFDM demodulation, channel estimation, and CIRs and channel parameters extraction; (3) storing the CIRs and channel parameters in the SSD; (4) system parameter configuration, device control, and graphical data visualization.

The core board of the system is shown in Figure 9, and the external interfaces of the system are shown in Figure 9. As shown in the figure, the developed system features high integration and is easy to deploy. And the performance parameters of the system are listed in Table 3.



(**a**) (**b**)

Figure 9. Core board and external interfaces. (**a**) Core board (**b**) External interfaces.

Table 3. Performance parameters of the 5G network monitoring system.

Parameters	Values
Frequency Range	10 MHz–6 GHz
Number of the ADC Channels	8
Maximum Measurement Bandwidth	1 GHz
Flatness within Bandwidth	±2 dB
Inter-channel Clock Synchronization Error	≤300 ns
Input Signal Dynamic Range	>40 dB
Minimum Measurement Interval Time	66.7 μs

6. Experimental Results

As shown in Figure 10, experiments were conducted based on a hardware-in-loop testbench in the laboratory. The 5G-R core network and base stations are all actual devices. The Spirent's Vertex channel emulator can accurately simulate the complex network conditions in the real environment, which can support up to 64 unidirectional RF channels with a frequency range from 30 MHz to 5925 MHz and up to 200 MHz bandwidth.

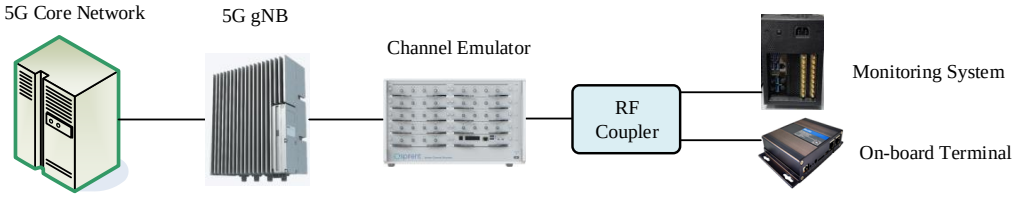


Figure 10. The architecture of the hardware-in-loop testbench.

6.1. Field Strength

In our experiment, the network monitoring system monitors the varying field strength, and compare the measurement results with that of the spectrum analyzer. To minimize measurement errors, each measurement result is the average of 100 independent measurements with systematic errors corrected.

As shown in Table 4, the maximum error of the measurement results is only 0.16 dB, over 90% of the measurement errors are less than 0.1 dB. Figure 11 shows the distribution of 100 measured values under the condition that the field strength is −51.10 dBm. It can be observed that the measurement error approximately follows a normal distribution, and the proportion of measurement results within the range of ±0.1 dB relative to the theoretical value reaches 80%. Consequently, the proposed system exhibits high accuracy comparable to that of the spectrum analyzer.

Table 4. Measurement results of field strength.

No.	Field Strength (dBm)	Monitoring System		Spectrum Analyzer	
		Measurement Result (dBm)	Error (dB)	Measurement Result (dBm)	Error (dB)
1	−6.10	−6.06	0.04	−6.25	−0.15
2	−11.10	−11.09	0.01	−11.02	0.08
3	−16.10	−16.07	0.03	−16.15	−0.05
4	−21.10	−21.10	0.00	−21.11	−0.01
5	−26.10	−26.16	−0.06	−26.04	0.06
6	−31.10	−31.16	−0.06	−31.18	−0.08
7	−36.10	−36.11	−0.01	−36.16	−0.06
8	−41.10	−41.16	−0.06	−41.15	−0.05
9	−46.10	−46.04	0.06	−46.05	0.05
10	−51.10	−51.15	−0.05	−50.96	0.14
11	−56.10	−55.94	0.16	−56.00	0.10

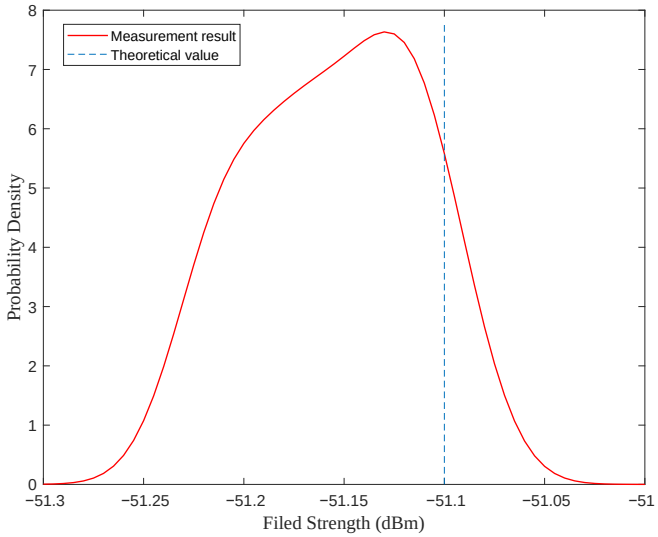


Figure 11. Probability density of field strength measurement results.

6.2. Multipath

(1) Multipath Delay and Power

The setting values in the Vertex channel emulator and the measurement values of the network monitoring system are shown in Table 5. The measured values of the relative delay and relative power are both the average values of 300 measurement samples.

Table 5. Multipath measurement results.

No.	Setting Value			Measured Value		Error	
	Relative Delay (μs)	**Relative Power (dB)**	**Fading Distribution**	**Relative Power (dB)**	**Relative Power (dB)**	**Delay Error (μs)**	**Power Error (dB)**
1	0	0	Rayleigh	0	0	0	0
2	0.8	−3	Rayleigh	0.798	−2.52	0.002	0.48
3	1.6	−6	Rayleigh	1.595	−5.82	0.005	0.18
4	2.4	−9	Rayleigh	2.400	−9.08	0	0.08

As can be seen from the table, the measured values of the multipath delay and power are highly consistent with the set values. The maximum relative power error is 0.48 dB, and the maximum relative delay error is 5 ns.

Figure 12 illustrates the magnitude fading distribution of the measured signals, which exhibits a high degree of consistency with the Rayleigh fading model configured by the Vertex channel emulator.

(2) Delay Resolution and Maximum Measurable Delay

High-speed railway scenarios exhibit significant complexity and diversity. In certain scenarios (e.g., large-scale railway stations), multipath components are dense, with extremely small relative delays between multipath; by contrast, in other scenarios (e.g., railway viaducts), multipath components are sparse, while there may exist multipath with extremely large delays.

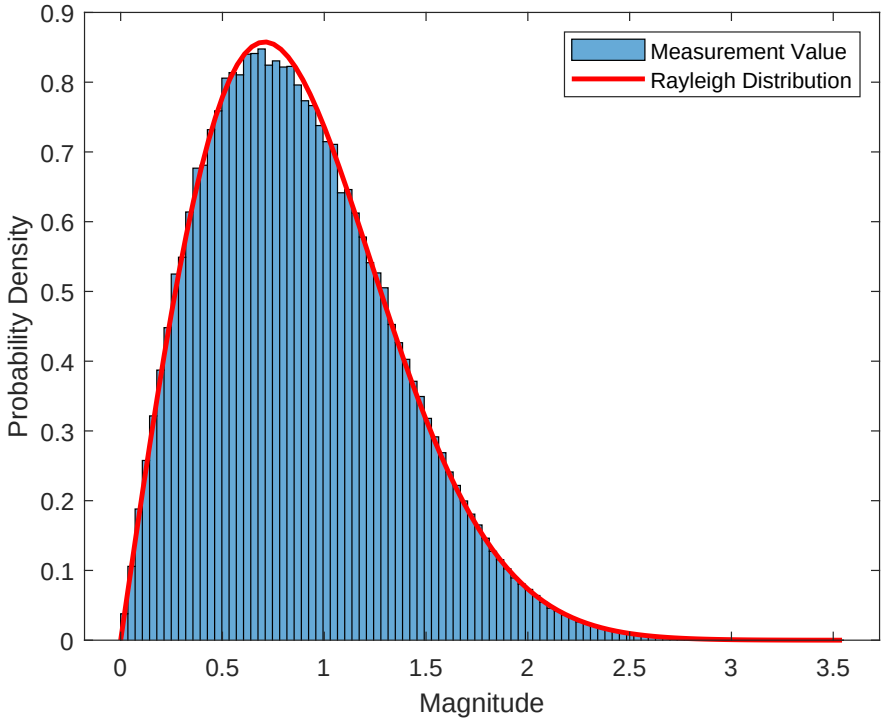


Figure 12. Fading distribution of measured received signals.

This subsection presents the experimental results of the delay resolution (i.e., minimum resolvable delay) and maximum measurable delay of the monitoring system, both of which are critical performance indicators of the system.

In the experiment, a two-path channel model was employed with relative delay ranging from 10 ns to 99 µs. Table 6 shows the measured and set delay. Theoretically, the delay resolution $\Delta\tau$ is inversely proportional to signal bandwidth B, $\Delta\tau = 1/B$. Although the system bandwidth B is set to 100 MHz, the actual occupied bandwidth is less due to the roll-off. Therefore, the delay resolution will be slightly greater than 10 ns. As shown in Table 6, the measured delay resolution conforms to the theoretical value.

It should be noted that 99 µs is the maximum delay supported by the Vertex channel emulator, and the maximum measurable delay of the system will exceed this value.

Table 6. Delay resolution and maximum measurable delay measurement results.

Set Relative Delay (µs)	Measured Relative Delay (µs)	Delay Error (ns)
0.01	Unresolvable	—
0.02	0.0163	−3.7
0.03	0.0244	−5.6
0.05	0.0488	−1.2
0.1	0.0977	−2.3
99	98.999	1.0

6.3. Frequency Offset

Table 7 compares the frequency offset measurement results with the theoretical values, where the measurement results are the average of 300 measurements. As can be seen from the table, the maximum measurement error of the frequency offset does not exceed 5 Hz.

Table 7. Frequency offset measurement results.

No.	Theoretical Value of Frequency Offset (Hz)	Measured Value of Frequency Offset (Hz)	Measurement Error of Frequency Offset (Hz)
1	97.2	101.0	3.8
2	388.9	388.8	−0.1
3	680.6	678.3	−2.3
4	875.0	875.3	0.3
5	972.2	977.0	4.8
6	1166.7	1163.6	−3.1
7	1555.6	1522.0	−3.6

7. Conclusions and Future Work

This paper proposes a network condition monitoring technology based on the DM-RS. By measuring and extracting the characteristics of the generalized channel, the monitoring of the RAN and the on-board terminal is achieved. Based on the RFSoC chip, this paper has completed the development of the system. The system not only has excellent performance and is easy to upgrade, but can also be deployed on high-speed trains for a long time. The performance of the 5G network monitoring system is tested. The experimental results show that the system can accurately measure the network metrics such as the field strength, multipath delay, and frequency offset. Validation in real High-Speed Railway (HSR) fault scenarios, integration into on-board terminals, and development of practical equipment for deployment on HSR are important tasks to be carried out in the future.

Author Contributions: Conceptualization, C.L. and D.F.; methodology, C.L. and P.R.; software, P.R.; validation, C.L. and P.R.; formal analysis, C.L. and D.F.; investigation, D.F.; resources, B.A. and L.X.; data curation, D.F. and P.R.; writing—original draft preparation, C.L. and P.R.; writing—review and editing, C.L. and L.X.; visualization, L.X.; supervision, B.A.; project administration, B.A. and L.X.; funding acquisition, C.L. and L.X. All authors have read and agreed to the published version of the manuscript.

Funding: This research was funded by the Fundamental Research Funds for the Central Universities (Grant No.: 2025JBMC021), the National Natural Science Foundation of China (Grant No.: U21A20445 and 62001135), the State Key Laboratory of Advanced Rail Autonomous Operation (Grant No.: RAO2023ZZ004).

Data Availability Statement: Data are contained within the article.

Conflicts of Interest: The authors declare no conflicts of interest.

Abbreviations

The following abbreviations are used in this manuscript:

5G	Fifth-Generation
DM-RSs	Demodulation Reference Signals
RFSoC	Radio Frequency System on Chip
FRMCS	Future Railway Mobile Communication System
EU	European Union
UIC	International Union of Railways
IoT	Internet of Things
KRRI	Korea Railroad Research Institute
RAN	Radio Access Network
CIT	Comprehensive Inspection Train

SNCF	French National Railway Company
MGV	Manned Ground Vehicle
I/Q	In-phase/Quadrature
PSS	Primary Synchronization Signal
SSS	Secondary Synchronization Signal
PBCH	Physical Broadcast Channel
PDSCH	Physical Downlink Shared Channel
PDCCH	Physical Downlink Control Channel
CIR	Channel impulse response
IFFT	Inverse Fast Fourier Transform
RSS	Received Signal Strength
IF	Intermediate Frequency
LO	Local Oscillator
ADC	Analog-to-Digital Converter
DDC	Digital Down Conversion
RAM	Random Access Memory
PCIe	Peripheral Component Interconnect Express
CTF	Channel Transfer Function
PLL	Phase Locked Loop
DC	Direct Current
PDM	Power Design Manager
SSD	Solid State Disk

References

1. Phusakulkajorn, W.; Núñez, A.; Wang, H.; Jamshidi, A.; Zoeteman, A.; Ripke, B.; Dollevoet, R.; De Schutter, B.; Li, Z. Artificial intelligence in railway infrastructure: Current research, challenges, and future opportunities. *Intell. Transp. Infrastruct.* **2023**, *2*, liad016. [CrossRef]
2. Ai, B.; Guan, K.; Rupp, M.; Kürner, T.; Cheng, X.; Yin, X.F.; Wang, Q.; Ma, G.; Li, Y.; Xiong, L.; et al. Future Railway Services-Oriented Mobile Communications Network. *IEEE Commun. Mag.* **2015**, *53*, 78–85. [CrossRef]
3. Guan, K.; Guo, X.; He, D.; Svoboda, P.; Berbineau, M.; Wang, S.; Ai, B.; Zhong, Z.; Rupp, M. Key technologies for wireless network digital twin towards smart railways. *High-Speed Railw.* **2024**, *2*, 1–10. [CrossRef]
4. He, R.; Ai, B.; Wang, G.; Guan, K.; Zhong, Z.; Molisch, A.F.; Briso-Rodriguez, C.; Oestges, C.P. High-Speed Railway Communications: From GSM-R to LTE-R. *IEEE Veh. Technol. Mag.* **2016**, *11*, 49–58. [CrossRef]
5. Sniady, A.; Sonderskov, M.; Soler, J. VoLTE Performance in Railway Scenarios: Investigating VoLTE as a Viable Replacement for GSM-R. *IEEE Veh. Technol. Mag.* **2015**, *10*, 60–70. [CrossRef]
6. International Union of Railways (UIC). *Future Railway Mobile Communication System (FRMCS)*; International Union of Railways (UIC): Paris, France, 2024. Available online: https://css0.uic.org/IMG/pdf/frmcs-t_v1_0_.pdf (accessed on 28 October 2025).
7. FRMCS Functional Working Group & Architecture and Technology Group. *Future Railway Mobile Communication System User Requirements Specification*; International Union of Railways: Paris, France, 2019; pp. 1–521.
8. Ai, B.; Molisch, A.F.; Rupp, M.; Zhong, Z.D. 5G Key Technologies for Smart Railways. *Proc. IEEE* **2020**, *108*, 856–893. [CrossRef]
9. Chen, R.; Long, W.X.; Mao, G.; Li, C. Development Trends of Mobile Communication Systems for Railways. *IEEE Commun. Surv. Tutor.* **2018**, *20*, 3131–3141. [CrossRef]
10. Vassiliki, N.; Dan, M.; Farid, B.; Michael, K.; Sébastien, T.; Bernd, H.; Guillaume, J.; Nazih, S.; Marion, B.; Stefanos, G. 5GRAIL paves the way to the Future Railway Mobile Communication System Introduction. In Proceedings of the 2022 IEEE Future Networks World Forum (FNWF), Montreal, QC, Canada, 12–14 October 2022; pp. 53–57. [CrossRef]
11. He, R.; Ai, B.; Zhong, Z.; Yang, M.; Chen, R.; Ding, J.; Ma, Z.; Sun, G.; Liu, C. 5G for Railways: Next Generation Railway Dedicated Communications. *IEEE Commun. Mag.* **2022**, *60*, 130–136. [CrossRef]
12. Xu, T.; Tang, T.; Gao, C. Dependability analysis of the data communication system in train control system. *Sci. China Ser. E-Technol. Sci.* **2025**, *52*, 2605–2618. [CrossRef]
13. Sun, B.; Guo, Y.; Yu, Y.; Liu, J.; Ai, B.; Zhong, Z.; Sun, X.; Wang, W. Reliability Analysis of CTCS-3 Train-Ground Communication System Based on 5G-R. *IEEE Trans. Veh. Technol.* **2023**, *72*, 12927–12940. [CrossRef]
14. Boutouchent, A.; Meridja, A.N.; Kardjadja, Y.; Maia, A.M.; Ghamri-Doudane, Y.; Koudil, M.; Glitho, R.H.; Elbiaze, H. AMANOS: An Intent-Driven Management and Orchestration System for Next-Generation Cloud-Native Networks. *IEEE Commun. Mag.* **2024**, *62*, 42–49. [CrossRef]

15. Archana, T.; Deepika, V.; Arjun Kumar, A.; Ramachandran, M.; Sivalingam, K.M.; Babu Narayanan Koonampilli, J. CygNet MaSoN: Analytics and Machine Learning Enabled Management System for 5G Networks. In Proceedings of the 2021 International Conference on COMmunication Systems & NETworkS (COMSNETS), Bangalore, India, 5–9 January 2021; pp. 94–96. [CrossRef]
16. Ramachandran, M.; Archana, T.; Deepika, V.; Kumar, A.A.; Sivalingam, K.M. 5G Network Management System with Machine Learning Based Analytics. *IEEE Access* **2022**, *10*, 73610–73622. [CrossRef]
17. Panek, M.; Jabłoński, I.; Woźniak, M. Automatic Performance Assessment—Step Toward Autonomous Mobile Network Management Systems. *IEEE Commun. Mag.* **2025**, *63*, 73–79. [CrossRef]
18. Weston, P.; Roberts, C.; Yeo, G.; Stewart, E. Perspectives on railway track geometry condition monitoring from in-service railway vehicles. *Veh. Syst. Dyn.* **2015**, *53*, 1063–1091. [CrossRef]
19. Hisa, T.; Kanaya, M.; Sakai, M.; Hamaoka, K. Rail and contact line inspection technology for safe and reliable railway traffic. *Hitachi Rev.* **2012**, *61*, 325–330.
20. Wang, H.; Silvast, M.; Markine, V.; Wiljanen, B. Analysis of the Dynamic Wheel Loads in Railway Transition Zones Considering the Moisture Condition of the Ballast and Subballast. *Appl. Sci.* **2017**, *7*, 1208. [CrossRef]
21. Jing, G.; Qin, X.; Wang, H.; Deng, C. Developments, challenges, and perspectives of railway inspection robots. *Autom. Constr.* **2022**, *138*, 104242. [CrossRef]
22. Kaliorakis, N.; Sakellariou, J.S.; Fassois, S.D. On-Board Random Vibration-Based Robust Detection of Railway Hollow Worn Wheels Under Varying Traveling Speeds. *Machines* **2023**, *11*, 933. [CrossRef]
23. Traquinho, N.; Vale, C.; Ribeiro, D.; Meixedo, A.; Montenegro, P.; Mosleh, A.; Calçada, R. Damage Identification for Railway Tracks Using Onboard Monitoring Systems in In-Service Vehicles and Data Science. *Machines* **2023**, *11*, 981. [CrossRef]
24. Dai, P.; Li, H.; Wang, F.; Tian, X.; Wang, H.; Xu, X. Key technologies of China high speed comprehensive inspection train: CIT450. *Railw. Eng. Sci.* **2025**, *33*, 414–440. [CrossRef]
25. Guan, K.; Peng, B.; He, D.; Eckhardt, J.M.; Yi, H.; Rey, S.; Ai, B.; Zhong, Z.; Kürner, T. Channel Sounding and Ray Tracing for Intrawagon Scenario at mmWave and Sub-mmWave Bands. *IEEE Trans. Antennas Propag.* **2021**, *69*, 1007–1019. [CrossRef]
26. Wang, W. Research on 5G-R Network Characteristics and Network Planning Techniques for Railways. *China Railw.* **2022**, *9*, 38–46.
27. Liu, X.; Tang, P.; Zhang, J.; Xu, Z.; Chang, Z.; Miao, H.; Ma, Z. Measurement and Simulation-Based Channel Characterization in Extra-Wagon Scenarios for 5G-R Communications. *IEEE Trans. Veh. Technol.* **2025**, 1–15. [CrossRef]
28. *ETSI TS 138 104*; 3GPP TS 38.104 Base Station (BS) Radio Transmission and Reception (Version 18.10.0). ETSI: Valbonne, France, 2025.
29. Minucci, F.; Verbruggen, D.; Sallouha, H.; Volski, V.; Vandenbosch, G.; Bovet, G.; Pollin, S. Measuring 5G Electric Fields Strength with Software Defined Radios. *IEEE Open J. Commun. Soc.* **2022**, *3*, 2258–2271. [CrossRef]
30. Qahtan Wali, S.; Sali, A.; Šuka, D.; Aerts, S.; Alkurayşi, M.; Li, L.; Ismail, A.; Hashim, F.; Alsaidosh, Y.A.; Gil Jiménez, V.P.; et al. An Assessment of Extrapolated Field Strengths Versus Distance, Measurement Time, and Induced Traffic from 5G Base Station in C-Band. *IEEE Access* **2024**, *12*, 130639–130653. [CrossRef]
31. Zhou, T.; Qiao, Y.; Salous, S.; Liu, L.; Tao, C. Machine Learning-Based Multipath Components Clustering and Cluster Characteristics Analysis in High-Speed Railway Scenarios. *IEEE Trans. Antennas Propag.* **2022**, *70*, 4027–4039. [CrossRef]
32. Xu, J.; Ai, B.; Chen, L.; Pei, L.; Li, Y.; Nazaruddin, Y.Y. When High-Speed Railway Networks Meet Multipath TCP: Supporting Dependable Communications. *IEEE Wirel. Commun. Lett.* **2020**, *9*, 202–205. [CrossRef]
33. You, Y.H.; Song, H.K. Efficient Sequential Detection of Carrier Frequency Offset and Primary Synchronization Signal for 5G NR Systems. *IEEE Trans. Veh. Technol.* **2020**, *69*, 9212–9216. [CrossRef]
34. Zhang, C.; Wang, G.; Jia, M.; He, R.; Zhou, L.; Ai, B. Doppler Shift Estimation for Millimeter-Wave Communication Systems on High-Speed Railways. *IEEE Access* **2019**, *7*, 40454–40462. [CrossRef]
35. Siafarikas, D.; Volakis, J.L. Toward Direct RF Sampling: Implications for Digital Communications. *IEEE Microw. Mag.* **2020**, *21*, 43–52. [CrossRef]
36. Gomez, R. Theoretical Comparison of Direct-Sampling Versus Heterodyne RF Receivers. *IEEE Trans. Circuits Syst. I Regul. Pap.* **2016**, *63*, 1276–1282. [CrossRef]

Disclaimer/Publisher's Note: The statements, opinions and data contained in all publications are solely those of the individual author(s) and contributor(s) and not of MDPI and/or the editor(s). MDPI and/or the editor(s) disclaim responsibility for any injury to people or property resulting from any ideas, methods, instructions or products referred to in the content.